Solar Energy 185 (2019) 1–12

Contents lists available at ScienceDirect

Solar Energy

journal homepage: www.elsevier.com/locate/solener

Introduction of co-additives to form well dispersed photoactive layer to improve performance and stability of organic solar cells

Jun Young Choi, Yong Woon Han, Sung Jae Jeon, Eui Jin Ko, Doo Kyung Moon*

Nano and Information Materials Laboratory (NIMs Lab.), Department of Chemical Engineering, Konkuk University, 120, Neungdong-ro, Gwangjin-gu, Seoul 05029, Republic of Korea

ARTICLE INFO

Keywords:
Organic solar cells
Co-additives
Well-distributed photoactive layer
Fullerene system
Non-fullerene system
Stability

ABSTRACT

We fabricated organic solar cells (OSCs) based on bulk-heterojunction photoactive layers with fullerene (PTB7:$PC_{71}BM$) and non-fullerene (PBDB-T:ITIC) systems by introducing 1,8-diiodooctane (DIO) and 4-fluorobenzaldehyde (4-FBA) as co-additives, respectively. Introduction of the co-additives led to a uniform surface morphology of photoactive layer and formed well distributed interpenetrating networks between donors and acceptors. Carrier recombination were reduced due to the favorable structure for charge transport. Consequently, the devices with co-additives achieved an enhanced performance with a PCE of 8.5% (J_{SC} = 16.4 mA/cm^2 and FF = 68.3%) in the fullerene system, and a PCE of 10.1% (J_{SC} = 16.9 mA/cm^2 and FF = 67.8%) in the non-fullerene system. In addition, the devices with co-additives showed improved stabilities compared to those with single additives. Correspondingly, the reduction ratio of PCE at ambient atmosphere conditions decreased from 17.07% to 10.59% in the fullerene system, and 34.02% to 24.75% in the non-fullerene system.

1. Introduction

Organic solar cells (OSCs), which are solution processable, have been attracting increased attention as next-generation solar cells because they offer numerous advantages, such as flexibility, low cost, light weight, and large fabrication areas via roll-to-roll processes (Han et al., 2018b; Park et al., 2009; Zhao et al., 2016a). The methods used to achieve high-power conversion efficiency (PCE) in these OSCs include the design of new donor/acceptor materials to increase low-carrier mobility and the low-absorption coefficient of the organic semiconductors (Bin et al., 2018; Jeon et al., 2018), and the use of interfacial engineering to increase the charge collection based on energy level alignment (Choi et al., 2016; Lee et al., 2016a; Xu et al., 2016). Moreover, the method of controlling the morphology by introducing additives to achieve high stability is an important issue as well (Kim et al., 2015; Lou et al., 2011; Qin et al., 2017).

For the photoactive layers of OSCs, a bulk heterojunction (BHJ) structure based on polymer donor and fullerene acceptor has been studied (Han et al., 2016; Lee et al., 2015; Liu et al., 2010). Generally, a fullerene acceptor, such as [6,6]-phenyl-C_{71}-butyric acid methyl ester ($PC_{71}BM$), have high-electron affinity and electron mobility. The fullerene acceptor was blended with (poly[[4,8-bis[(2-ethylhexyl)oxy] benzo[1,2-b:4,5-b']dithiophene-2,6-diyl][3-fluoro-2-[(2-ethylhexyl) carbonyl]thieno[3,4-b]thiophenediyl]] (PTB7)—a polymer donor with a low bandgap—the PCE exceeded 9% (He et al., 2012; Wienk et al., 2003). However, fullerene derivatives have limited bandgap control and low absorption properties in the visible light region. Moreover, because of their strong intermolecular attraction, they exhibit a tendency to easily aggregate in the presence of heat, which limits their ability to function as acceptors for high-performance OSCs (An et al., 2018; Chao et al., 2016). Recently, non-fullerene acceptors have been actively researched to overcome the problems associated with fullerene acceptor (Kini et al., 2018; Meng et al., 2016). 3,9-bis(2-methylene-(3-(1,1-dicyanomethylene)-indanone))-5,5,11,11-tetrakis(4-hexylphenyl)-dithieno[2,3-d:2′,3′-d']-s-indaceno[1,2-b:5,6-b']dithiophene (ITIC), a typical non-fullerene acceptor, is a small molecule that can easily control molecular energy levels. In addition, it exhibits increased short circuit current density owing to its long-wavelength absorption properties (Lin et al., 2015). According to literature, blending ITIC with the polymer donor poly[(2,6-(4,8-bis(5-(2-ethylhexyl)thiophen-2-yl)-benzo [1,2-b:4,5-b']dithiophene))-alt-(5,5-(1′,3′-di-2-thienyl-5′,7′-bis(2-ethylhexyl)benzo[1′,2′-c:4′,5′-c']dithiophene-4,8-dione))] (PBDB-T) resulted in a PCE that exceeded 11% (Zhao et al., 2016b). Accordingly, both fullerene and non-fullerene systems can enhance device performance and stability by optimizing the photoactive layer morphology through microstructure control, such as solvent vapor annealing, and the

* Corresponding author.
E-mail address: dkmoon@konkuk.ac.kr (D.K. Moon).

https://doi.org/10.1016/j.solener.2019.03.093
Received 21 December 2018; Received in revised form 7 March 2019; Accepted 28 March 2019
Available online 17 April 2019

introduction of additives (Kwon et al., 2017; Lee et al., 2017; Moulé and Meerholz, 2009; Sun et al., 2017).

Therefore, the morphology of the photoactive layer has a considerable effect on the efficiency and stability. Accordingly, to control the morphology, it becomes necessary to control the phase separation of the polymer donor and acceptor (Bi et al., 2018; Cha et al., 2018; Yan et al., 2018). Solvents with high boiling points, such as 1,8-diiodooctane (DIO), diphenyl ether (DPE), and chloronaphthalene (CN), are typically used as additives to control morphology (Collins et al., 2013; Kwon et al., 2015; Zheng et al., 2016). Furthermore, studies have been conducted on the use of 4,4′-biphenol (BPO) and $(HxN_3)_2$-SiPc as the third component used to enhance the PCE and stability of photoactive layer (Cheng et al., 2016; Grant et al., 2017). Meanwhile, DIO has a higher selective solubility toward the acceptor than the donor. Consequently, it is the most extensively used additives as it is capable of nanoscale phase separation based on the formation of donor and acceptor domains (Sai-Anand et al., 2018). In the fullerene system, most of optimum concentration of the processing additives was found to be 2–3% v/v that enhanced the aggregation of the polymer but reduced the fullerene domain size. It can improve the carrier mobility as it facilitates the molecular packing (Ren et al., 2011; Song et al., 2018). On the other hand, most of optimum concentration of the processing additives was found to be less than 0.5% v/v that enhanced the crystalline content and the domain size in the non-fullerene system. The reason of the performance drops at concentration above 0.5% v/v is that forms a large-scale phase separation of donors and acceptors which has a negative effect on charge transport and collection (Chen et al., 2019). However, because residual additives in the photoactive layer can cause photodegradation, processes such as methanol treatment and vacuum treatment are necessary (Tremolet De Villers et al., 2016; Ye et al., 2013).

Chen et al. (2017) used 2-chlorobenzaldehyde (2-CBA) with a low-boiling point in their study on fast removable solvent additives that did not require vacuum drying. The boiling point of 2-CBA (211.9 °C) with polar functional groups was lower than that of DIO (332.5 °C), but higher than the main solvent chlorobenzene (131 °C). Furthermore, it had a higher solubility property for the acceptor compared to the donor. Such characteristics allow the microstructure of the photoactive layer to be controlled, and also serve as an alternative to DIO, which requires the removal of residual additives.

In addition, Aïch et al. (2014) and Oseni and Mola (2017) reported that it was possible to control the acceptor domain and nanoscale morphology of the photoactive layer by using a co-additives system based on two types of solvent additives. Such a system results in improved charge extraction by reducing carrier recombination (Wan et al., 2016; Ye et al., 2012).

Accordingly, OSCs based on a co-additives system that simultaneously introduces two additives with different boiling points can improve charge transport properties by controlling the microstructure of the photoactive layer.

In the present study, we fabricated OSCs with an inverted structure by introducing a co-additives system using DIO and 4-fluorobenzaldehyde (4-FBA) to the photoactive layer. We also evaluated the performance and stability according to changes in the morphology of the photoactive layer in the fullerene (PTB7:PC_{71}BM) and non-fullerene systems (PBDB-T:ITIC), respectively. Herein, 4-FBA which was introduced as co-additives could control the morphology by forming well-distributed donors and acceptors within the photoactive layer. As a result, there was an increase in the interpenetrating networks. The reduction in the charge trap site in the co-additives system was confirmed by atomic force microscopic (AFM) analysis. Moreover, X-ray photoelectron spectroscopy (XPS), cross-sectional scanning electron microscopy (SEM), and contact angle analysis, were used to confirm that the photoactive layer with well-distributed donor and acceptor had been formed. This resulted in the formation of a favorable structure for improving the charge transport properties, while J_{SC} and FF also improved. Consequently, improved PCE of 8.5% and 10.1% were achieved in the fullerene and non-fullerene systems, respectively. Moreover, the performance of the fullerene system with co-additives showed decreased by the reduction of V_{OC} and J_{SC} (PCE = from 8.5% to 7.9%, rate of decrease = 7.06%), after 350 h of storage at ambient atmosphere conditions. Similarly, the performance of the non-fullerene system with co-additive showed decreased by the reduction in J_{SC} and FF (PCE = from 10.1% to 8.6%, rate of decrease = 14.85%). These results revealed that devices with co-additives were more stable that those with a single additives.

2. Experimental

2.1. Materials

PTB7 and PC_{71}BM, which were used as donor and acceptor in the fullerene system, were purchased from 1-Material (Canada). PBDB-T, used as donor of the non-fullerene system, was synthesized in our group by reference to the synthesis method of Qian et al. (2012). In addition, ITIC used as acceptor was purchased from Derthon (China). Chlorobenzene (CB, 99.8%) used as the main solvent, and 1,8-diiodooctane (DIO, 98%) and 4-fluorobenzaldehyde (4-FBA, 98%) used as solvent additives were purchased from Sigma Aldrich (USA).

2.2. Preparation of photoactive solution

The photoactive solution of fullerene system were formed at 1:1.5 ratio of PTB7 and PC_{71}BM which dissolved in CB(DIO, 3% v/v) solution of single additives system or CB(DIO, 3% v/v + 4-FBA, 0.5% v/v) solution of co-additives system. The photoactive solution of non-fullerene system were formed at 1:1 ratio of PBDB-T and ITIC which dissolved in CB(DIO, 0.5% v/v) solution of single additives system or CB(DIO, 0.5% v/v + 4-FBA, 0.2% v/v) solution of co-additives system. The solutions were then used after 8 h of stirring at 40 °C and 50 °C, respectively.

2.3. Device fabrication

To fabricate the inverted OSCs device, ITO glass was cleaned by ultra-sonication using acetone, neutral detergent, isopropyl alcohol, deionized water in sequence, after that, UVO cleaning (Ahtech LTS AH 1700) was performed. After cleaning, zinc oxide (ZnO) sol-gel precursor was spin-coated in ambient condition and annealed at 200 °C to form the 30 nm thick of electron transporting layer (ETL). Prepared PTB7:PC_{71}BM solution of the fullerene system was spin coated, and dried for one hour in N_2-filled glove box to form the 100 nm thick layer. Prepared PBDB-T:ITIC solution of the non-fullerene system were spin coated and the film annealed at 160 °C to form the 100 nm thick layer. MoO_3 (5 nm) and Ag (100 nm) anodes formed 0.04 cm^2 electrodes using the thermal evaporation with high-vacuum chamber (less than 1×10^{-6} torr).

2.4. Device characterization

The current density (J) – voltage (V) characteristics of fabricated OSCs were measured by Keithley 2400 source measure unit and an AM 1.5G solar simulator (Oriel, 1000w). The incident photon-to-current conversion (IPCE) was measured to determine the external quantum efficiency (EQE) using the Polaronix K3100 IPCE measurement system (Mc science). The electrostatic potential (ESP) of DIO and 4-FBA used as the solvent additives were calculated through the Hartree-Fock 3-21G method of Gaussian 09. The atomic force measurement (AFM) was used PSIA XE-100 to measure the morphology of the photoactive layer. The electrochemical impedance spectroscopy (EIS) was measured in Z-θ mode for a varying frequency (from 500 Hz to 1 MHz) with an AC drive bias of 25 mV. To determine the atomic concentration of the photoactive layer surface, the X-ray photoelectron spectroscopy (XPS) was

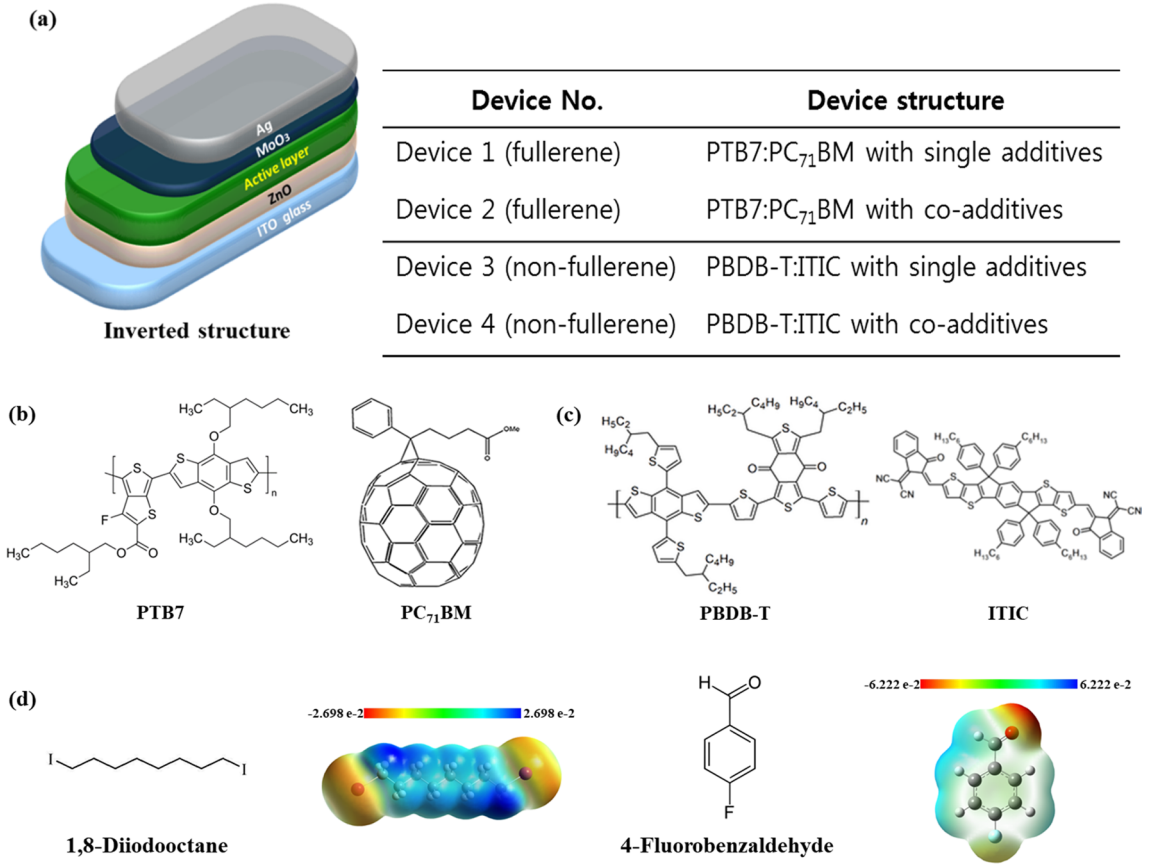

Device No.	Device structure
Device 1 (fullerene)	PTB7:$PC_{71}BM$ with single additives
Device 2 (fullerene)	PTB7:$PC_{71}BM$ with co-additives
Device 3 (non-fullerene)	PBDB-T:ITIC with single additives
Device 4 (non-fullerene)	PBDB-T:ITIC with co-additives

Fig. 1. Schematic image of (a) Organic solar cells device structure and, chemical structure of (b) PTB7 and $PC_{71}BM$, (c) PBDB-T and ITIC, (d) 1,8-Diiodooctane and 4-Fluorobenzaldehyde.

measured using the PHI 5000 VersaProbe. To determine the atomic distribution of the photoactive layer, the energy dispersive X-ray spectra (EDS) mapping method of the scanning electron microcopy (SEM) was measured using the SU8010 FE-SEM (Hitachi). The contact angle and surface energy characteristics were measured and calculated using the contact angle analyzer (DSA100, KRUSS). The electron and hole mobilities were calculated using the SCLC method. In addition, UV absorption property was measured using Agilent 8453 and photoluminescence was measured using Perkin Elmer LS55.

3. Results and discussion

Fig. 1 shows the structure of the fabricated device and the polymer donor and acceptor materials used on the photoactive layer. The fabricated device had an inverted structure (ITO/ZnO/photoactive layer/MoO_3/Ag) (in Fig. 1(a)). For the fabrication of the device, chlorobenzene (boiling point = 131 °C) was used as the solvent. For both the fullerene and non-fullerene systems, DIO was used as the single additives, while DIO and 4-FBA were used together as the co-additives. For the photoactive layers, a BHJ structure with a mixture of a fullerene acceptor ($PC_{71}BM$) and PTB7 (Fig. 1(b)), and a BHJ structure with a mixture of a non-fullerene acceptor (ITIC) and PBDB-T (Fig. 1(c)), were used for the fullerene and non-fullerene systems, respectively. Fig. 1(d) shows the molecular structure and electrostatic potential (ESP) of DIO (boiling point = 332.5 °C) and 4-FBA (boiling point = 181 °C), which were used as solvent additives. According to the solubility results reported, DIO exhibits a very low solubility in polymer donors, and relatively higher solubilities in the fullerene and non-fullerene acceptors (Lee et al., 2016b; Zheng et al., 2018). Fig. S1 shows the solubility properties of DIO and 4-FBA, which were additives of PTB7 and $PC_{71}BM$ (fullerene system, Fig. S1(a)), and PBDB-T and ITIC (non-fullerene system, Fig. S1(b)). As shown in Fig. S1, the additives DIO and 4-FBA had higher solubility properties to the acceptors ($PC_{71}BM$ and ITIC) than the donor (PTB7 and PBDB-T). In particular, $PC_{71}BM$ exhibited improved solubilities in both DIO and 4-FBA, whereas ITIC exhibited higher solubilities in 4-FBA. As confirmed by ESP, 4-FBA exhibited higher acceptor solubility than DIO owing to the large and strong polarization from the increased electronegativity of the fluorine that was substituted on the benzene ring.

Fig. 2 and Table 1 show the current density-voltage (J-V) characteristics, external quantum efficiency (EQE) characteristics, and photovoltaic properties of the fabricated devices. In the fullerene systems, Device 1 showed a maximum PCE of 8.2% (J_{SC} = 16.0 mA/cm^2, V_{OC} = 0.757 V, and FF = 67.5%) with the use of a single additives. By contrast, Device 2 which used co-additives, achieved a PCE of 8.5% (J_{SC} = 16.4 mA/cm^2, V_{OC} = 0.757 V, and FF = 68.3%). In the non-fullerene systems, Device 3, which used a single additives, showed a PCE of 9.7% (J_{SC} = 16.8 mA/cm^2, V_{OC} = 0.878 V, and FF = 65.4%), whereas Device 4 which used co-additives achieved a PCE of 10.1% (J_{SC} = 16.9 mA/cm^2, V_{OC} = 0.878 V and FF = 67.8%). In conclusion, both fullerene (J_{SC}: from 16.0 mA/cm^2 to 16.4 mA/cm^2, FF: from 67.5% to 68.3%) and non-fullerene (J_{SC}: from 16.8 mA/cm^2 to 16.9 mA/cm^2, FF: from 65.4% to 67.8%) systems achieved improved PCE due to improvements in J_{SC} and FF. According to a study by Lou et al. (2011) on the effects of additives, the introduction of solvent additives can change the domain size of the donor and acceptor based on phase separation. Additionally, Kim et al. (2013) also reported that the introduction of additives can lead to a well-distributed phase, which can facilitate more balanced charge transport. In addition, Aïch et al. (2012) demonstrated that the morphology of the photoactive layer can be controlled by co-additives. Similarly, the introduction of 4-FBA as a co-additives caused changes in the domain size of fullerene and non-fullerene systems and

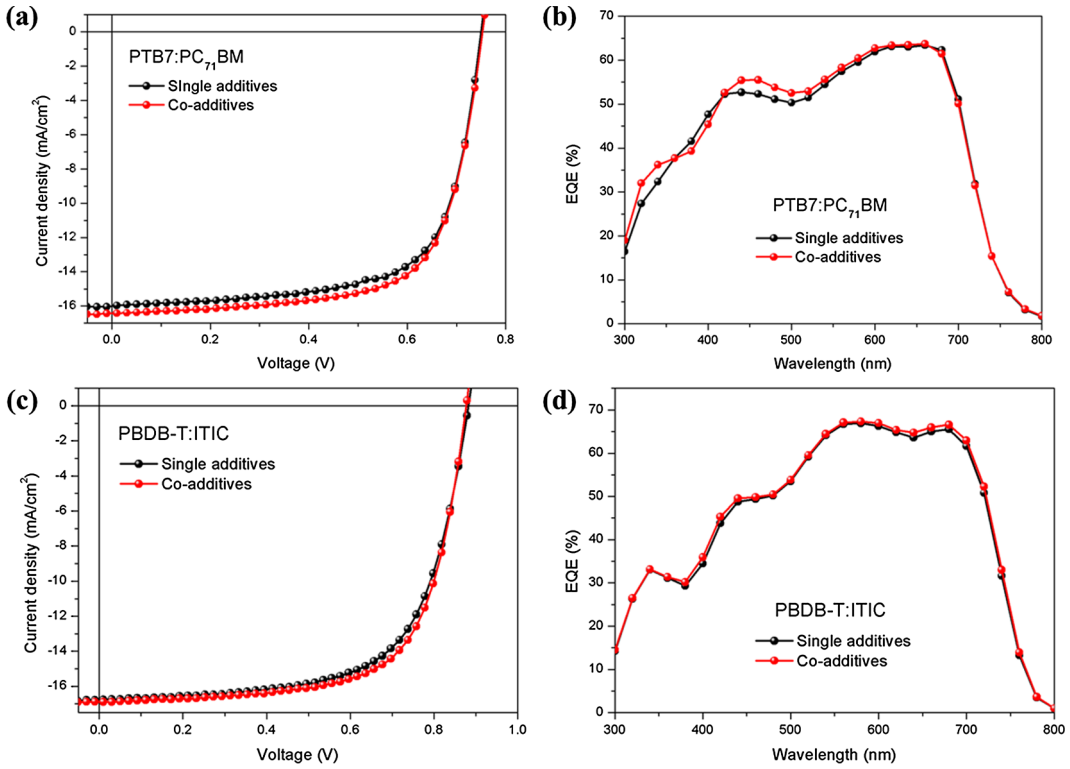

Fig. 2. Current density-voltage (J-V) characteristics and EQE spectra of (a), (b) fullerene system devices and (c), (d) non-fullerene system devices.

helped form a well-distributed photoactive layer that resulted in an increased J_{SC} due to the improved charge transport. This also led to a decrease in the carrier recombination, which caused an increase in FF. As a result, the PCE improved.

Tables S1 and S2 shows the photovoltaic properties according to the co-additives used. The devices shown in Tables S1 were fabricated with the ratio of DIO matched the best performance conditions (Table 1), while the ratio of 4-FBA was altered. In the fullerene system, compared to the device with single additives, the device with co-additives of 0.5% v/v 4-FBA achieved the highest PCE, which was attributed to an increase of FF. However, J_{SC} improved as the ratio of 4-FBA increased, but V_{OC} and FF tended to decrease, which resulted in a lower PCE. In the non-fullerene system, the device with co-additives of 0.2% v/v 4-FBA exhibited an improved PCE owing to an increase in FF compared to that with the single additives. At 0.5% v/v, the results showed a more decreases in FF than increases in J_{SC}. As shown, when the ratio of 4-FBA was increased, decreases in FF caused excessive phase separation. The devices shown in Tables S2 were fabricated with fixed ratio of 4-FBA, while the ratio of DIO was altered. The optimized DIO uses 3% v/v in the fullerene system, and 0.5% v/v in the non-fullerene system. In the fullerene system, the device with co-additives of 0.5% v/v 4-FBA achieved the highest PCE, which was attributed to an increase of FF. However, J_{SC} improved as the ratio of 4-FBA increased, but V_{OC} and FF tended to decrease, which resulted in a lower PCE.

Fig. 3 shows the morphological characteristics of the film with the single additives or co-additives in the fullerene and non-fullerene systems immediately (Fig. 3(a)–(d)) and at 10 days (Fig. 3(e)–(h)) after coating. The fabricated films used the same photoactive layer as Devices 1–4. In the fullerene system, the root-mean-square (RMS) roughness of the single additives was 0.656 nm (Fig. 3(a)). The RMS roughness of the co-additives showed similar morphological properties with 0.673 nm, however, the co-additives exhibited increased uniformity (Fig. 3(b)). In the non-fullerene system, the RMS roughness of the single additives was 1.751 nm (Fig. 3(c)), whereas the co-additives formed a relatively uniform film (Fig. 3(d)) with an RMS roughness of 1.276 nm. Both the fullerene and non-fullerene systems formed sharp agglomerates when single additives were introduced, but when co-additives were introduced, they formed domains with an excellent donor and acceptor phase separation. The sharp agglomerates found in the fullerene and non-fullerene systems with single additives can act as carrier trap sites increasing carrier recombination. Meanwhile, the introduction of co-additives formed excellent phase separation, which contributed to increased charge transport by the formation of interpenetrating networks. Similar to the findings of Ma et al. (2005), increased charge transport occurred because of the formation of interpenetrating networks. Fig. 3(e)–(h) and Tables S3 show morphological characteristics and photovoltaic performance measured after 10 days of storage at ambient atmosphere conditions, as shown in Fig. 3(a)–(d). In the fullerene system, the morphology of photoactive layer with single additives and co-additives became rougher after 10 days compared to their states immediately after fabrication with the RMS roughness increasing from 0.656 nm to 2.502 nm (Fig. 3(a), (e)) and from 0.673 nm

Table 1
Photovoltaics properties of fullerene system devices and non-fullerene system devices.

Device No.	Active layer	Additives	V_{OC} [V]	J_{SC} [mA/cm^2]	FF [%]	PCE [a] (PCE$_{max}$) [%]	R_s [Ω cm^2]	R_{sh} [Ω cm^2]
Device 1	PTB7:PC$_{71}$BM	Single	0.757 ± 0.02	16.0 ± 0.3	67.5 ± 0.9	8.03 (8.2)	5.12	639.6
Device 2		Co (4-FBA 0.5% v/v)	0.757 ± 0.02	16.4 ± 0.3	68.3 ± 0.4	8.33 (8.5)	4.78	762.8
Device 3	PBDB-T:ITIC	Single	0.878 ± 0.01	16.8 ± 0.4	65.4 ± 0.7	9.56 (9.7)	6.87	924.8
Device 4		Co (4-FBA 0.2% v/v)	0.878 ± 0.01	16.9 ± 0.3	67.8 ± 0.6	9.99 (10.1)	5.64	976.8

[a] The average PCE values and standard deviation are based on over 10 devices.

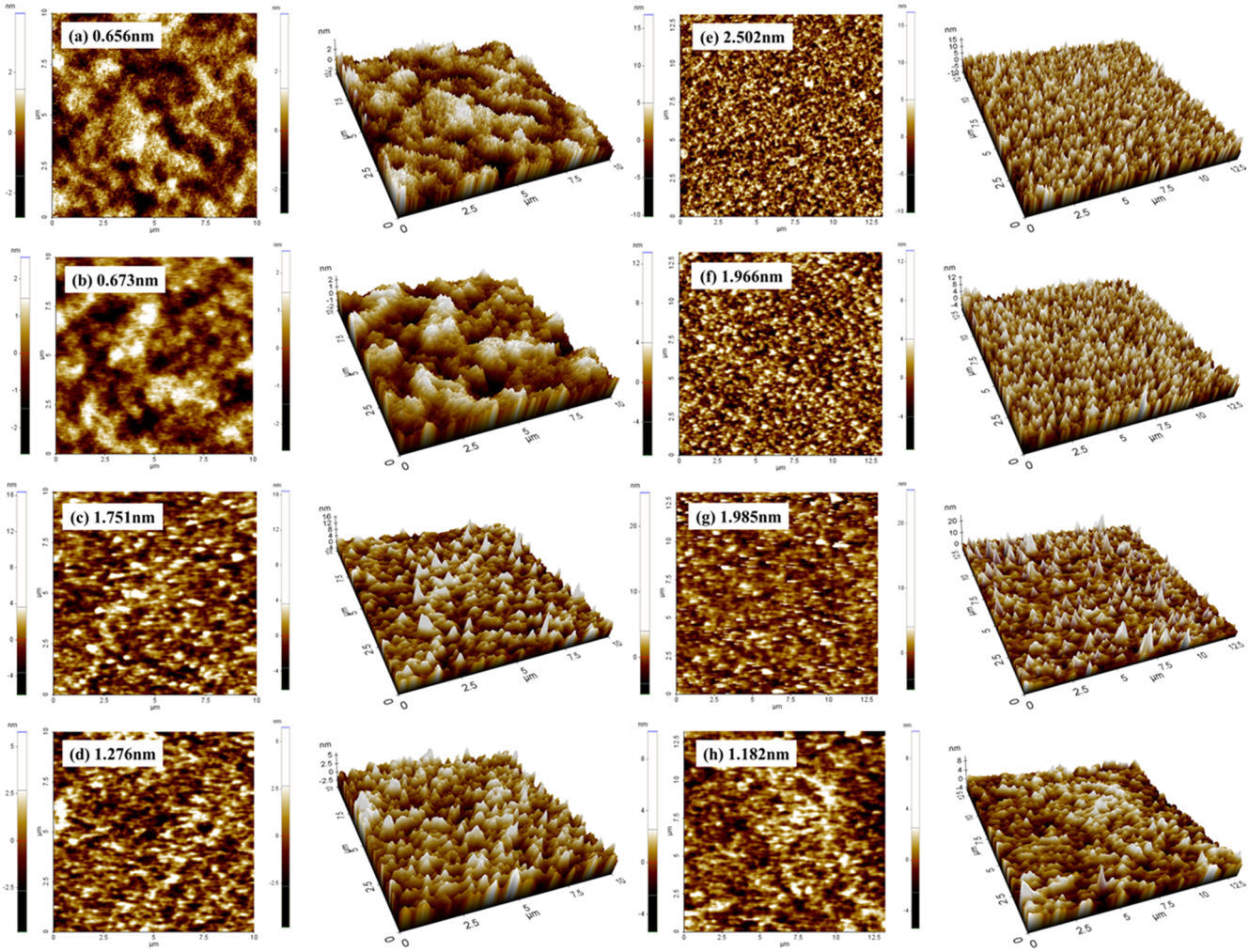

Fig. 3. Initial and after 10 days AFM image of (a), (e) fullerene system single additives photoactive layer, (b), (f) fullerene system co-additives photoactive layer, (c), (g) non-fullerene system single additives photoactive layer and (d), (h) non-fullerene system co-additives photoactive layer.

to 1.966 nm (Fig. 3(b), (f)), respectively. Introduction of co-additives resulted in relatively uniform morphological properties after 10 days. In the non-fullerene system, single additives showed a rougher morphology after 10 days as compared to immediately after fabrication, furthermore, the RMS roughness increased from 1.751 nm to 1.985 nm (Fig. 3(c), (g)). In contrast, co-additives showed uniform morphological properties, and the RMS roughness decreased from 1.276 nm to 1.182 nm (Fig. 3(d), (h)). The introduction of single additives resulted in an aggregation over time that increased the RMS roughness of the film, but the introduction of co-additives prevented aggregation which resulted in the formation of a uniform morphology. This was due to the introduction of co-additives at ambient atmosphere conditions and the elicited phase-freezing effect. As shown in Tables S3, in the fullerene system, Device 1 (single additives) and Device 2 (co-additives) showed decreases in PCE of 12.2% (from 8.2% to 7.2%) and 7.06% (from 8.5% to 7.9%), respectively. Such results were primarily due to decreases in V_{OC} and J_{SC}. Meanwhile, in the non-fullerene system, Device 3 (single additives) and Device 4 (co-additives) showed decreases in PCE of 21.65% (from 9.7% to 7.6%) and 14.85% (from 10.1% to 8.6%), respectively. Such results were primarily due to decreases in J_{SC} and FF.

Fig. S2 shows the dark current density–voltage characteristics of the fabricated initial devices (Devices 1–4) and after 10 days of storage at ambient atmosphere conditions. As shown in Fig. S2(a) and (b), in both the fullerene and non-fullerene systems, the initial devices with co-additives have low leakage current density in the reverse bias region and high current density in the forward bias region, as compared to the initial devices with single additives. This demonstrated that J_{SC} and FF increased due to an increase in the charge transport and a reduction in carrier recombination. This tendency is consistent with the results shown in Fig. 2 and Table 1. On the other hand, both single additives and co-additives devices after 10 days have reduced current density in the forward bias region, as compared to the initial devices. J_{SC} and FF of the devices after 10 days were reduced. Nevertheless, co-additives devices after 10 days have less reduction as compared to the single additives devices, resulting in more stable. Meanwhile, in the fullerene systems, the devices after 10 days have increased leakage current density in the reverse bias region. According to literature, the leakage current has a related to V_{OC}, and a decrease in V_{OC} can occur as the leakage current increases through the shockley equation (He et al., 2010). This tendency is consistent with the results shown in Fig. 3 and Tables S3.

Fig. S3. and Tables S4 show the electrochemical impedance spectroscopy (EIS) characteristics of the initial devices (Device 1–4) and the devices after 10 days. The Niquist plots were fitted by using the equivalent circuit modeling of an ohmic series resistance (R_1) in series with a charge transport resistance (R_2) in parallel (Zhou et al., 2013). R_1 was contributed from the electrical contacts and the sheet resistance of the electrodes. R_2 was contributed from the charge transport resistance inside the photoactive layer and the interface with electrodes (Wan et al., 2016). As shown in Fig. S3(a), Device 2 (co-additives) showed a decreased in R_1 (from 33.64 Ω cm^2 to 29.89 Ω cm^2) and R_2 (from 55.11 Ω cm^2 to 52.44 Ω cm^2) compared to Device 1 in the

Table 2
Surface atomic concentration of fullerene system and non-fullerene system photovoltaics.

Active layer	Additives	C_{1s} [%]	O_{1s} [%]	S_{2p} [%]	F_{1s} [%]	N_{1s} [%]	C/S ratio
PTB7:$PC_{71}BM$	Single	87.37	6.66	4.5	1.47	.	19.41
	Co	87.1	6.82	4.64	1.44	.	18.77
PBDB-T:ITIC	Single	89.82	4.03	5.56	.	0.59	16.17
	Co	88.07	4.36	6.12	.	1.45	14.39

fullerene system. Similarly, as shown in Fig. S3(b), Device 4 (co-additives) showed a decreased in R_1 (from 51.82 Ω cm^2 to 48.44 Ω cm^2) and R_2 (from 75.47 Ω cm^2 to 73.37 Ω cm^2) compared to Device 1 in the non-fullerene system. Decreased R_2 was attributed to an increase charge transfer occurred with the introduction of co-additives. These results are consistent with the trend of the series resistance (R_s) and shunt resistance (R_{sh}) in Table 1 which were calculated from the reciprocals of the slopes of the J-V characteristics at I = 0 mA/cm^2 and V = 0 V (Liao et al., 2013). On the other hand, as shown in Tables S4, both fullerene system and non-fullerene system devices after 10 days showed increased in R_1 and R_2 compared to initial devices. The increased R_2 of the devices after 10 days were due to the aggregation over time as shown in Fig. 3. Nevertheless, R_2 of the co-additives devices after 10 days were relatively less increased than single additives devices. This was due to the introduction of co-additives elicited phase-freezing effect.

Figs. 4 and S4 show the surface X-ray photoelectron spectroscopy (XPS) characteristics of the photoactive layer used in the fabrication of the devices. Table 2 shows the atomic concentrations calculated by XPS analysis. In general, surface analysis by XPS analysis can be used to analyze substances that contain specific atoms (Cheng et al., 2018). As shown in Fig. 1(a) and (b), the atomic signals were analyzed by targeting C, O, S, and F atoms in the fullerene system and C, O, S, and N atoms in the non-fullerene system. Fig. 4(a) shows the XPS survey spectra and Figs. 4(b), (c), S4(a) and (b) show the atomic signals of the single additives and co-additives used in the fullerene system. Herein, S_{2p} (at 164.6 eV and 163.6 eV) and F_{1s} (≈687.0 eV) signals were mostly due to PTB7, while C_{1s} (≈284.4 eV) and O_{1s} (≈532.4 eV) signals were mostly due to PTB7 and $PC_{71}BM$. As shown in Table 2, the C/S ratio of the atomic concentration decreased from 19.41% to 18.77% with co-additives, as compared to the use of the single additives. Based on these results, it was determined that using co-additives caused a greater increase in PTB7 and a decrease in $PC_{71}BM$ on the surface of the photoactive layer compared to the case where only single additives was used. Fig. 4(d) shows the XPS survey spectra and Figs. 4(e), (f), S4(c) and (d) show the atomic signals of the single additives and co-additives in the non-fullerene system. The N_{1s} (≈C≡N, 399 eV) signal was mostly attributed to ITIC, while C_{1s} (≈C−C, 284.8 eV, C═O 287.6), S_{2p} (≈C_4S–H (thiophene) 165 eV, 164 eV), and O_{1s} (≈531 eV, 532.3 eV) signals were mostly attributed to PBDB–T and ITIC. Similar to the fullerene system, the non-fullerene system also showed a decrease in the C/S atomic concentration ratio, from 16.17% to 14.39% with co-additives than with the single additives. This indicated that PBDB-T which has lower C/S atomic ratio increased on the surface of the photoactive layer, while ITIC decreased. This was because 4-FBA was introduced, as a results, PTB7 and PBDB-T were enriched on the top surface of the photoactive layer. According to literature, donor enriched on the anode caused by vertical phase separation in an inverted structure, it is advantageous for charge transport and reduced the carrier recombination (Xu et al., 2009). Consequently, the introduction of co-additives allowed the donor to be well-distributed on the top surface, which formed a structure favorable for charge transport within the photoactive layer and caused J_{SC} and FF to increase. This tendency was consistent with the results shown in Fig. 2 and Table 1.

Fig. 5 shows the water contact angle and surface energy properties of the photoactive layer film that were used in Devices 1–4. In the fullerene system, the contact angle and surface energy properties of the single additives photoactive film (Fig. 5(a)) were 92.5° and 16.88 mN/m, respectively, whereas those of the co-additives (Fig. 5(b)) were 93.0° and 16.57 mN/m, respectively. In the non-fullerene system, the contact angle and surface energy properties of the photoactive film with the single additives (Fig. 5(c)) were 100.2° and 12.5 mN/m, respectively, whereas those of co-additives (Fig. 5(d)) were 100.6° and 12.29 mN/m, respectively. In both the fullerene and non-fullerene systems, co-additives showed lower surface energies and high hydrophobic surface properties than single additives. In general, $PC_{71}BM$ has higher hydrophilic properties than other polymer donors, such as PTB7, and ITIC also had high hydrophilic properties than another polymer donor, such as PBDB-T. Consequently, polymer donor has higher water contact angle properties compared to $PC_{71}BM$ and ITIC (Cheng et al., 2015; Liu et al., 2018). Therefore, unlike the introduction of single additives, introduction of co-additives causes donor-enriched distributions within the photoactive layer. Correspondingly, as the quantity of acceptor decreased on the surface, it resulted in hydrophobic surface properties. Consequently, the donor and acceptor within the photoactive layer became well-distributed, which caused increases in the charge transport that contributed to the improvement of PCE. Such tendency is consistent with the results shown in Figs. 2–4.

Fig. 6 shows the results of the analysis of each atom within the photoactive layer using energy dispersive X-ray spectra (EDS) mapping and cross-sectional scanning electron microscopy (SEM) on Devices 1–4. Each sample was prepared with ITO (180 nm)/ZnO (30 nm)/photoactive layer (100–110 nm)/MoO_3 (5 nm)/Ag (100 nm). In the fullerene system (Fig. 6(a) and (b)), EDS mapping of the cross-sections for S, and F atoms, were analyzed to identify the distributions of PTB7 (S, F atoms). Moreover, in the non-fullerene system (Fig. 6(c) and (d)), EDS mapping of the cross-sections for S, and N atoms, were analyzed to identify the distributions of PBDB-T (S atoms) and ITIC (S, N atoms) (Fig. 6(c) and (d)). In the fullerene system, the mapping image for S signals showed that Device 2 (Fig. 6(b)) was more uniformly distributed than Device 1 (Fig. 6(a)). S signals may be used to identify the behavior of PTB7. Based on the results, PTB7 within the photoactive layer showed a well-distributed behavior when co-additives were used. Similarly, in the non-fullerene system, the mapping image of N signals showed that Device 4 (Fig. 6(d)) was more uniformly distributed than Device 3 (Fig. 6(c)). The behavior of ITIC was examined using N signals and the results confirmed that ITIC within the photoactive layer showed a well-distributed behavior when the co-additives were used. As both the fullerene and non-fullerene system showed well-distributed behaviors for the photoactive materials, it was determined that the carrier mobility was increased due to the formation of interpenetrating networks (Choi et al., 2015). Similar to the confirmation by the C/S ratios in XPS shown in Fig. 4, this tendency confirmed that co-additives were able to form a photoactive layer with a well-distributed donor and acceptor in both the fullerene and non-fullerene systems.

Fig. S5 and Table S5 shows the X-ray diffraction (XRD) characterization used to measure the crystallinity of fullerene and non-fullerene films. We used the Bragg's law to calculate the π-π stacking distance ($d_{(1\,0\,0)}$) and the lamellar distance ($d_{(1\,0\,0)}$) (Yu et al., 2019). Fig. S5(a) shows the out-of-plane patterns and Fig. S5(b) shows the in-plane patterns of the photoactive layer films used in the fullerene system. The single additives film presented a (0 1 0) peak at 2θ = 19.53° ($d_{(0\,1\,0)}$:

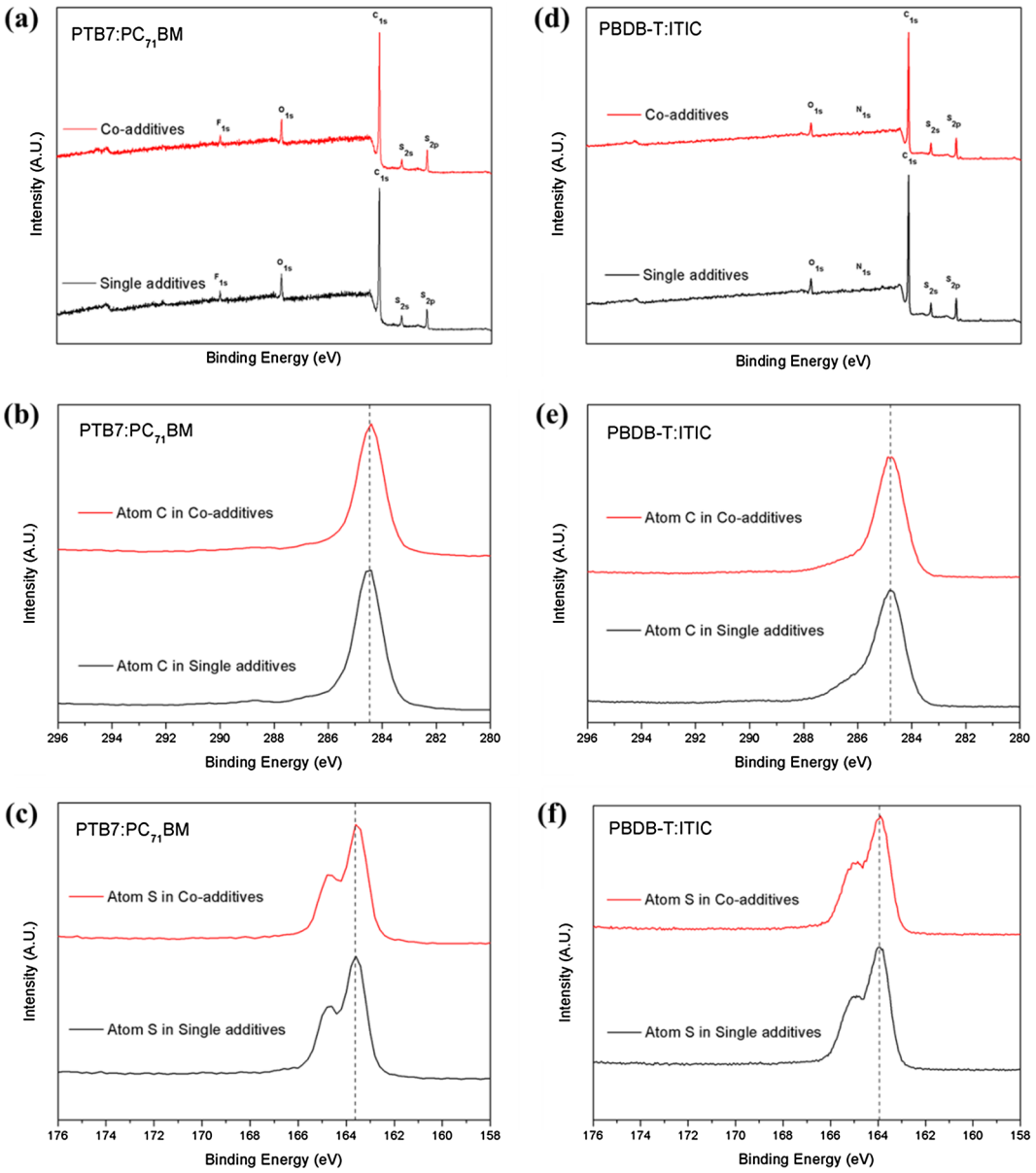

Fig. 4. XPS characteristics of (a), (d) surface and atomic signals of (b), (e) carbon, (c), (f) sulfur with respect to fullerene system and non-fullerene system.

0.45 nm) in out-of-plane direction and a (1 0 0) peak at 2θ = 3.24° ($d_{(1\,0\,0)}$: 2.73 nm) in in-plane direction. The co-additives film presented a (0 1 0) peak at 2θ = 20.62° ($d_{(0\,1\,0)}$: 0.43 nm) in out-of-plane direction and a (1 0 0) peak at 2θ = 3.19° ($d_{(1\,0\,0)}$: 2.77 nm) in in-plane direction. As a result, the co-additives films formed more improved π-π stacking strength and closed molecular stacking which formed the favorable structure for charge transport (Han et al., 2018a). Similarly, Fig. S5(c) show the out-of-plane patterns and Fig. S5(d) shows the in-plane patterns of the photoactive layer films used in the non-fullerene system. The single additives film presented a (0 1 0) peak at 2θ = 21.18° ($d_{(0\,1\,0)}$: 0.42 nm) in out-of-plane direction and a (1 0 0) peak at 2θ = 3.89° ($d_{(1\,0\,0)}$: 2.27 nm) in in-plane direction (Liang et al., 2018). The co-additives film presented a (0 1 0) peak at 2θ = 21.17° ($d_{(0\,1\,0)}$: 0.42 nm) in out-of-plane direction and a (1 0 0) peak at 2θ = 3.98° ($d_{(1\,0\,0)}$: 2.22 nm) in in-plane direction. As a result, the co-additives films formed similar π-π stacking strength, but a more improved closed molecular stacking which formed the favorable structure for charge transfer.

Fig. S6 shows the ultraviolet–visible (UV–vis) spectroscopy spectra of fullerene and non-fullerene films. In the fullerene system (Fig. S6(a)), the photoactive layer of co-additives showed increased absorption properties near λ = 450–700 nm, as compared to the cases where single additives were used. Similarly, in the non-fullerene system (in Fig. S6(b)), the co-additives in the photoactive layer showed increased absorption properties in all regions, as compared to the single additives case. This was due to the introduction of co-additives that caused phase separation in the photoactive layer morphology, which resulted in increased light absorption (Lee et al., 2008).

Fig. S7 shows the photoluminescence (PL) properties of fullerene and non-fullerene system films. Both the fullerene and non-fullerene systems showed a lower PL intensity with the introduction of co-additives compared to that of single additives. As shown in Fig. S6, both the fullerene and non-fullerene systems resulted in increased absorption properties with the introduction of co-additives compared to that of single additives. Consequently, in both systems, the carrier generation of the co-additives device increased due to improved absorption properties. However, lower emission properties were exhibited. This indicated that co-additives show decreased carrier recombination than single additives. These results were also indicative of the fact that co-additives formed well-distributed photoactive layer, which decreased

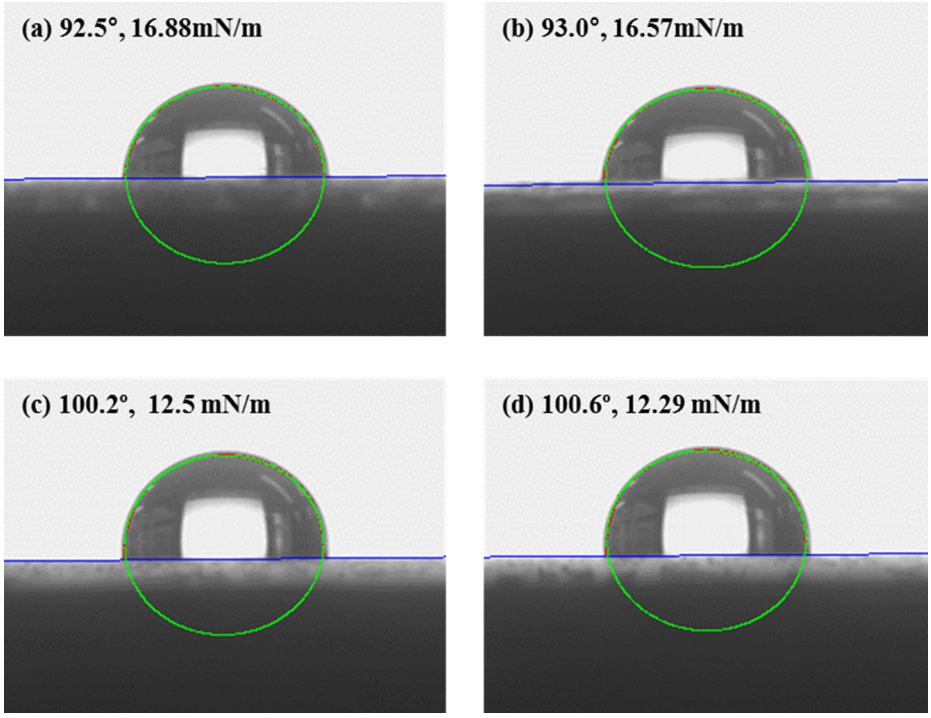

Fig. 5. Water contact angle of (a) fullerene system single additives photoactive layer, (b) fullerene system co-additives photoactive layer, (c) non-fullerene system single additives photoactive layer, (d) non-fullerene system co-additives photoactive layer.

carrier recombination by increasing charge transport, thereby contributing to the improvement of FF and PCE. Such tendency was consistent with the results shown in Figs. 3–6 and Table 1.

Fig. 7 and Table 3 show the electron and hole mobilities calculated by the space charge limited current (SCLC) method. To derive the electron and hole mobilities, an electron-only (ITO/ZnO/photoactive layer/LiF/Al) and hole-only devices (ITO/PEDOT:PSS/photoactive layer/MoO_3/Ag) were respectively fabricated. Electron and hole mobilities were calculated using the Mott–Gurney equation (Li et al., 2018; Sánchez et al., 2017), as shown below:

$$J = (9/8)\varepsilon_r\varepsilon_0\mu_{eff}(V^2/L^3) \quad (1)$$

where J is the current density, ε_r is the dielectric constant of the material, ε_0 is the dielectric constant of the permittivity of vacuum, μ_{eff} is the carrier mobility, V is the applied voltage, and L is the layer film thickness. Fig. 7(a) and (b) show the electron and hole mobilities of the

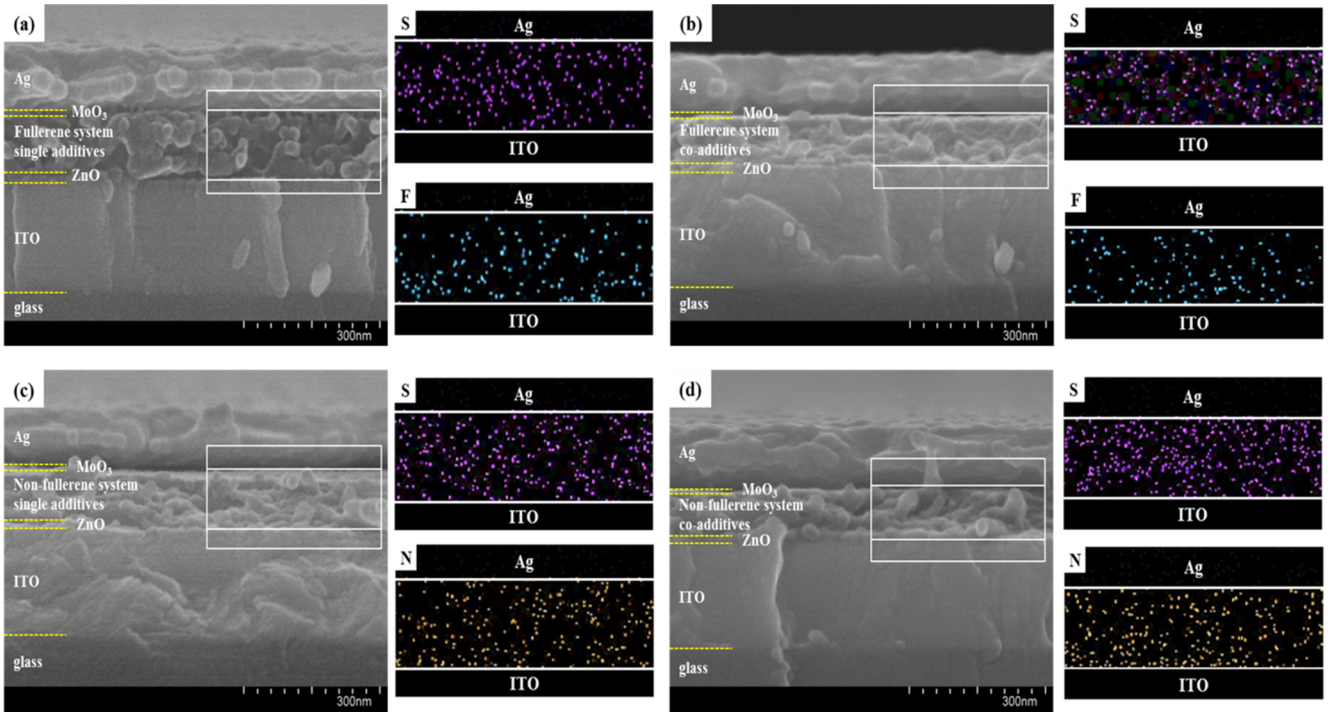

Fig. 6. Cross-sectional scanning electron microscope (SEM) image and energy dispersive X-ray spectra (EDS) mapping of each element in photoactive layer.

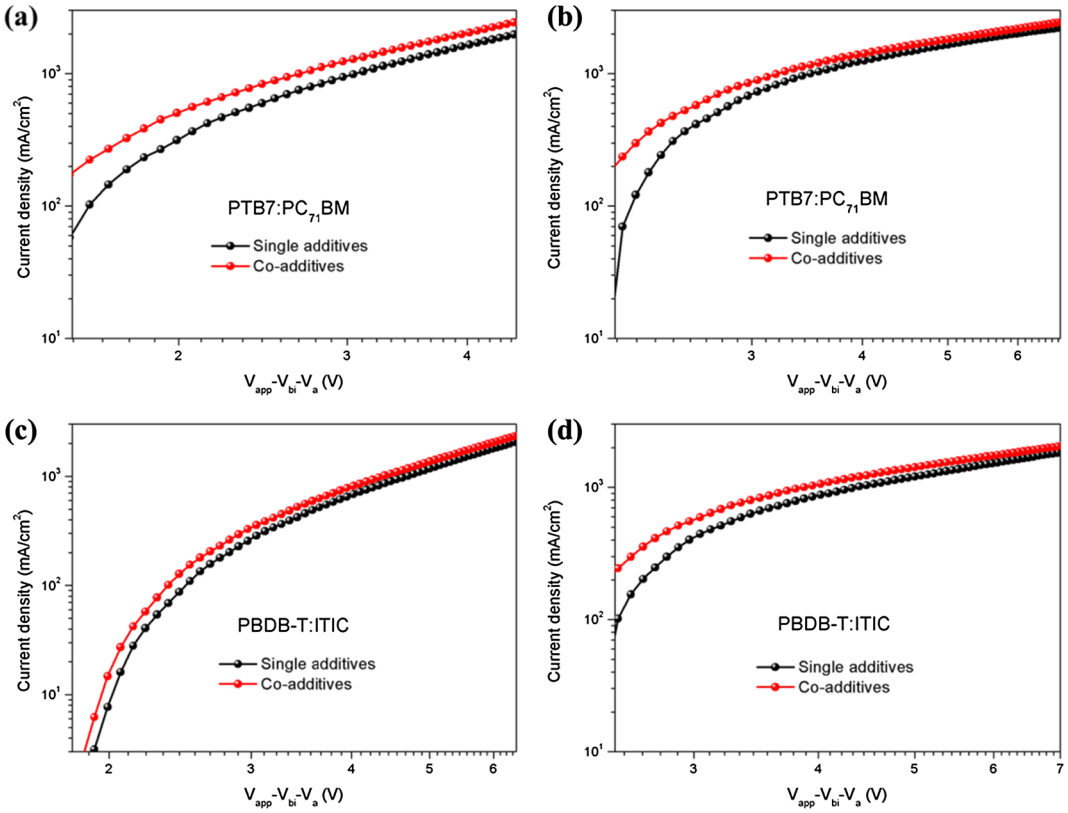

Fig. 7. SCLC characteristics of (a) fullerene system electron only device and (b) hole only device, (c) non-fullerene system electron only device and (d) hole only device.

Table 3
The carrier mobilities of fullerene system and non-fullerene system devices.

Device No.	Active layer	Additives	μ_e (cm^2/VS)	μ_h (cm^2/VS)
Device 1	PTB7:$PC_{71}BM$	Single	3.43×10^{-4}	2.40×10^{-4}
Device 2		Co	4.42×10^{-4}	2.97×10^{-4}
Device 3	PBDB-T:ITIC	Single	1.75×10^{-4}	1.64×10^{-4}
Device 4		Co	1.88×10^{-4}	2.20×10^{-4}

single additives and co-additives in the fullerene system. The calculated mobilities were as follows: $\mu_{e,\ single} = 3.43 \times 10^{-4}\,cm^2/Vs$, $\mu_{e,\ co} = 4.42 \times 10^{-4}\,cm^2/Vs$, $\mu_{h,\ single} = 2.4 \times 10^{-4}\,cm^2/Vs$, and $\mu_{h,\ co} = 2.97 \times 10^{-4}\,cm^2/Vs$. Fig. 7(c) and (d) respectively show the electron and hole mobilities of the single additives and co-additives in the non-fullerene system. The calculated mobilities were as follows: $\mu_{e,\ single} = 1.75 \times 10^{-4}\,cm^2/Vs$, $\mu_{e,\ co} = 1.88 \times 10^{-4}\,cm^2/Vs$, $\mu_{h,\ single} = 1.64 \times 10^{-4}\,cm^2/Vs$, and $\mu_{h,\ co} = 2.20 \times 10^{-4}\,cm^2/Vs$. When 4-FBA was introduced as co-additives, the hole and electron mobilities increased, as compared to the single additives. This enhancement was due to increased charge transport and balanced carrier mobility as a result of formed the photoactive layer with well-distributed donor and acceptor. Such a tendency is consistent with the results shown in Figs. 2–7.

Fig. 8 shows the stability properties of Devices 1–4 measured for 350 h at ambient atmosphere conditions without encapsulation. As shown in Fig. 8(a), the PCE of Device 1 decreased by 17.07%, from an initial value of 8.2% to 6.8%, while the PCE of Device 2 decreased by 10.59%, from an initial value of 8.5% to 7.6%. As shown in Fig. 8(b)–(d), the primary reasons for the decline in performance were the decreases in J_{SC} and FF for Device 1 and the decrease in J_{SC} for Device 2. In Fig. 8(e), the PCE of Device 3 decreased by 34.02%, from an initial value of 9.7% to 6.4%, while the PCE of Device 4 decreased by 24.75%, from an initial value of 10.1% to 7.6%. As shown in Fig. 8(f)–(h), the primary reason for the decline in performance were the decrease in J_{SC} and FF for Device 3, whereas Device 4 showed relatively small decreases. These results were similar to the AFM morphology of the photoactive layer measured after 10 days in ambient atmosphere conditions (Fig. 3). The introduction of the co-additives maintained the phase by preventing aggregation within the photoactive layer, thus resulting in decreased carrier trap sites due to the formation of a relatively uniform film compared to the single additives. These properties contributed to the improvement in J_{SC} and FF, and as a result, co-additives were able to exhibit a higher stability than single additives. Such tendency is highly consistent with the results of Figs. 2–7.

4. Conclusions

In this study, we successfully fabricated OSCs with the introduction of DIO and 4-FBA as co-additives in the photoactive layers of fullerene (PTB7:$PC_{71}BM$) and non-fullerene (PBDB-T:ITIC) systems. The photoactive layer exhibited a uniform morphology when co-additives were introduced. Moreover, because the introduction of co-additives allowed the formation of a well-distributed molecular order, the properties became more favorable for charge transport. Furthermore, there was a reduction in carrier recombination due to decreases in sharp agglomerates that acted as charge trap sites on the surface of the photoactive layer. Due to these effects, we were successful in fabricating devices with maximum PCE of 8.5% and 10.1% due to increases in J_{SC} and FF. When the stability of the devices at ambient atmosphere conditions was assessed, the reduction ratio of PCE decreased which ranged from 17.07% to 10.59% in the fullerene system, and from 34.02% to 24.75% in the non-fullerene system. This indicated significant improvements in stability due to the introduction of co-additives. The results of this study may contribute significantly to large area and mass production of OSCs.

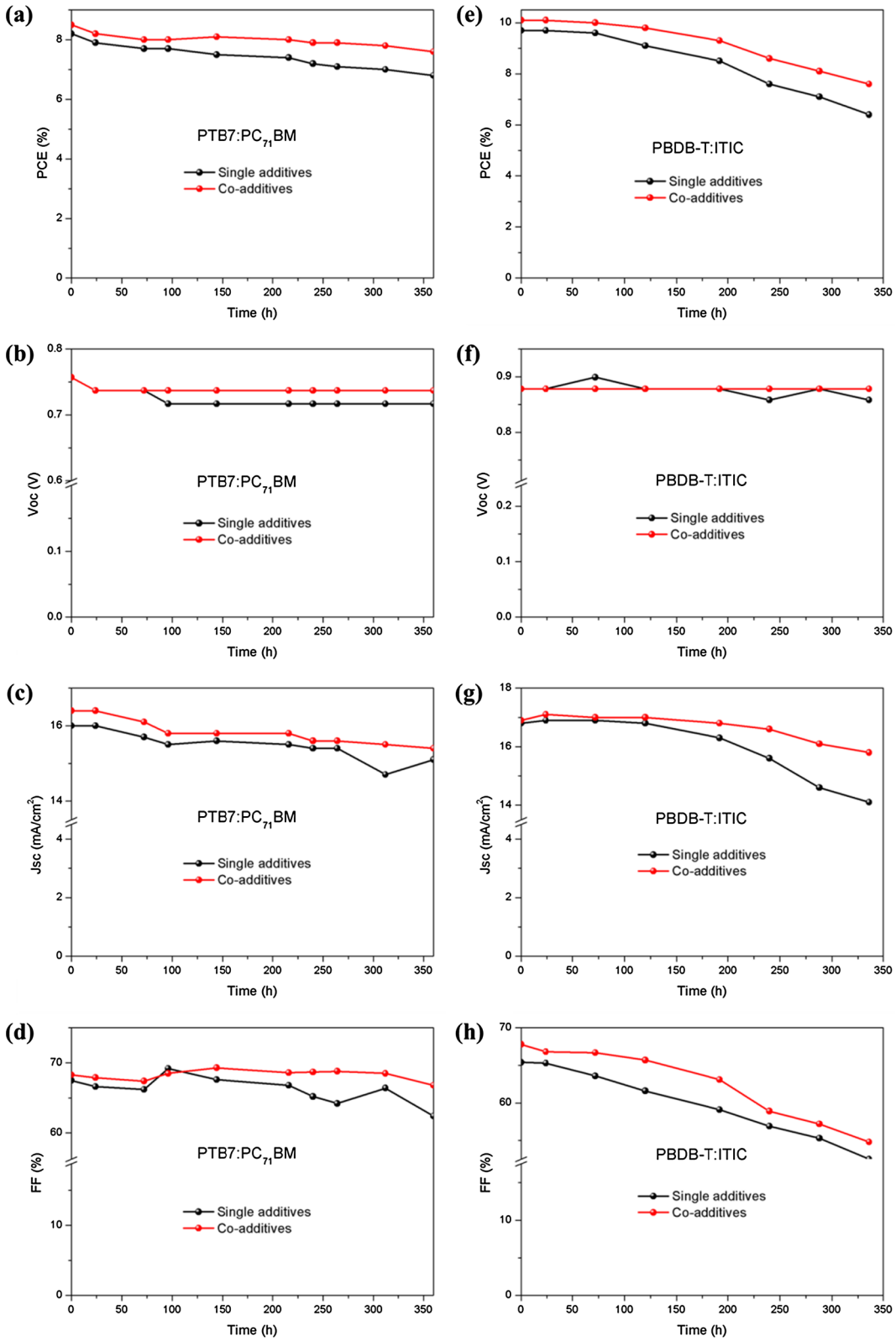

Fig. 8. Stability properties in ambient atmosphere of (a)–(d) fullerene system devices and (e)–(h) non-fullerene system devices.

Acknowledgments

This research was supported by New & Renewable Energy Core Technology Program of the Korea Institute of Energy Technology Evaluation and Planning (KETEP) grant funded by the Ministry of Trade, Industry & Energy (MI, Korea) (no. 20153010140030) and the Human Resources Program in Energy Technology of the Korea Institute of Energy Technology Evaluation and Planning (KETEP), granted financial resource from the Ministry of Trade, Industry & Energy, Republic of Korea (No. 20174010201540) and Korea Institute of Energy Technology Evaluation and Planning (KETEP). This paper was supported by Konkuk University Researcher Fund in 2017.

Appendix A. Supplementary material

Supplementary data to this article can be found online at https://doi.org/10.1016/j.solener.2019.03.093.

References

Aïch, B.R., Beaupré, S., Leclerc, M., Tao, Y., 2014. Highly efficient thieno[3,4-c]pyrrole-4,6-dione-based solar cells processed from non-chlorinated solvent. Org. Electron. Phys., Mater. Appl. 15, 543–548. https://doi.org/10.1016/j.orgel.2013.12.012.

Aïch, B.R., Lu, J., Beaupré, S., Leclerc, M., Tao, Y., 2012. Control of the active layer nanomorphology by using co-additives towards high-performance bulk heterojunction solar cells. Org. Electron. Phys. Mater. Appl. 13, 1736–1741. https://doi.org/10.1016/j.orgel.2012.05.001.

An, Q., Zhang, F., Gao, W., Sun, Q., Zhang, M., Yang, C., Zhang, J., 2018. High-efficiency and air stable fullerene-free ternary organic solar cells. Nano Energy 45, 177–183. https://doi.org/10.1016/j.nanoen.2017.12.050.

Bi, P., Xiao, T., Yang, X., Niu, M., Wen, Z., Zhang, K., Qin, W., So, S.K., Lu, G., Hao, X., Liu, H., 2018. Regulating the vertical phase distribution by fullerene-derivative in high performance ternary organic solar cells. Nano Energy 46, 81–90. https://doi.org/10.1016/j.nanoen.2018.01.040.

Bin, H., Yao, J., Yang, Y., Angunawela, I., Sun, C., Gao, L., Ye, L., Qiu, B., Xue, L., Zhu, C., Yang, C., Zhang, Z.G., Ade, H., Li, Y., 2018. High-efficiency all-small-molecule organic solar cells based on an organic molecule donor with alkylsilyl-thienyl conjugated side chains. Adv. Mater. 30, 1–8. https://doi.org/10.1002/adma.201706361.

Cha, H., Wheeler, S., Holliday, S., Dimitrov, S.D., Wadsworth, A., Lee, H.H., Baran, D., McCulloch, I., Durrant, J.R., 2018. Influence of blend morphology and energetics on charge separation and recombination dynamics in organic solar cells incorporating a nonfullerene acceptor. Adv. Funct. Mater. 28, 1–11. https://doi.org/10.1002/adfm.201704389.

Chao, Y.C., Chuang, C.H., Hsu, H.L., Wang, H.J., Hsu, Y.C., Chen, C.P., Jeng, R.J., 2016. Enhanced thermal stability of organic photovoltaics via incorporating triphenylamine derivatives as additives. Sol. Energy Mater. Sol. Cells 157, 666–675. https://doi.org/10.1016/j.solmat.2016.07.041.

Chen, J., Bi, Z., Xu, X., Zhang, Q., Yang, S., Guo, S., Yan, H., You, W., Ma, W., 2019. Fine optimization of morphology evolution kinetics with binary additives for efficient non-fullerene organic solar cells. Adv. Sci. 1801560, 1801560. https://doi.org/10.1002/advs.201801560.

Chen, J., Zhang, L., Jiang, X., Gao, K., Liu, F., Gong, X., Chen, J., Cao, Y., 2017. Using o-chlorobenzaldehyde as a fast removable solvent additive during spin-coating PTB7-based active layers: high efficiency thick-film polymer solar cells. Adv. Energy Mater. 7, 1–8. https://doi.org/10.1002/aenm.201601344.

Cheng, P., Wang, R., Zhu, J., Huang, W., Chang, S.Y., Meng, L., Sun, P., Cheng, H.W., Qin, M., Zhu, C., Zhan, X., Yang, Y., 2018. Ternary system with controlled structure: a new strategy toward efficient organic photovoltaics. Adv. Mater. 30, 1–8. https://doi.org/10.1002/adma.201705243.

Cheng, P., Yan, C., Lau, T.K., Mai, J., Lu, X., Zhan, X., 2016. Molecular lock: a versatile key to enhance efficiency and stability of organic solar cells. Adv. Mater. 2, 5822–5829. https://doi.org/10.1002/adma.201600426.

Cheng, P., Yan, C., Li, Y., Ma, W., Zhan, X., 2015. Diluting concentrated solution: a general, simple and effective approach to enhance efficiency of polymer solar cells. Energy Environ. Sci. 8, 2357–2364. https://doi.org/10.1039/c5ee01838b.

Choi, H., Ko, S.J., Kim, T., Morin, P.O., Walker, B., Lee, B.H., Leclerc, M., Kim, J.Y., Heeger, A.J., 2015. Small-bandgap polymer solar cells with unprecedented short-circuit current density and high fill factor. Adv. Mater. 27, 3318–3324. https://doi.org/10.1002/adma.201501132.

Choi, M.H., Lee, E.J., Han, J.P., Moon, D.K., 2016. Solution-processed pH-neutral conjugated polyelectrolytes with one-atom variation (O, S, Se) as a novel hole-collecting layer in organic photovoltaics. Sol. Energy Mater. Sol. Cells 155, 243–252. https://doi.org/10.1016/j.solmat.2016.06.017.

Collins, B.A., Li, Z., Tumbleston, J.R., Gann, E., Mcneill, C.R., Ade, H., 2013. Absolute measurement of domain composition and nanoscale size distribution explains performance in PTB7:PC71bm solar cells. Adv. Energy Mater. 3, 65–74. https://doi.org/10.1002/aenm.201200377.

Grant, T.M., Gorisse, T., Dautel, O., Wantz, G., Lessard, B.H., 2017. Multifunctional ternary additive in bulk heterojunction OPV: Increased device performance and stability. J. Mater. Chem. A 5, 1581–1587. https://doi.org/10.1039/c6ta08593h.

Han, Y.W., Choi, J.Y., Lee, Y.J., Ko, E.J., Choi, M.H., Suh, I.S., Moon, D.K., 2018a. Vertical phase separation for highly efficient organic solar cells incorporating conjugated-polyelectrolytes. Adv. Mater. Interfaces 6, 1801396. https://doi.org/10.1002/admi.201801396.

Han, Y.W., Jeon, S.J., Choi, J.Y., Kim, J.H., Moon, D.K., 2018b. Highly efficient ternary solar cells of 10.2% with core/shell quantum dots via FRET. Effect. Sol. RRL 1800077, 1800077. https://doi.org/10.1002/solr.201800077.

Han, Y.W., Lee, E.J., Joo, J., Park, J., Sung, T.H., Moon, D.K., 2016. Photon energy transfer by quantum dots in organic-inorganic hybrid solar cells through FRET. J. Mater. Chem. A 4, 10444–10453. https://doi.org/10.1039/c6ta02523d.

He, C., Zhong, C., Wu, H., Yang, R., Yang, W., Huang, F., Bazan, G.C., Cao, Y., 2010. Origin of the enhanced open-circuit voltage in polymer solar cells via interfacial modification using conjugated polyelectrolytes. J. Mater. Chem. 20, 2617. https://doi.org/10.1039/b921775d.

He, Z., Zhong, C., Su, S., Xu, M., Wu, H., Cao, Y., 2012. Enhanced power-conversion efficiency in polymer solar cells using an inverted device structure. Nat. Photonics 6, 591–595. https://doi.org/10.1038/nphoton.2012.190.

Jeon, S.J., Lee, T.H., Han, Y.W., Moon, D.K., 2018. Design and synthesis of 2D A1-π-A2copolymers impact on fullerene network for efficient polymer solar cells. Polym. (United Kingdom) 149, 85–95. https://doi.org/10.1016/j.polymer.2018.04.032.

Kim, W., Kim, J.K., Kim, E., Ahn, T.K., Wang, D.H., Park, J.H., 2015. Conflicted effects of a solvent additive on PTB7:PC71BM bulk heterojunction solar cells. J. Phys. Chem. C 119, 5954–5961. https://doi.org/10.1021/jp510996w.

Kim, Y., Yeom, H.R., Kim, J.Y., Yang, C., 2013. High-efficiency polymer solar cells with a cost-effective quinoxaline polymer through nanoscale morphology control induced by practical processing additives. Energy Environ. Sci. 6, 1909–1916. https://doi.org/10.1039/c3ee00110e.

Kini, G.P., Choi, J.Y., Jeon, S.J., Suh, I.S., Moon, D.K., 2018. Controlling the interchain packing and photovoltaic properties via fluorine substitution in terpolymers based on benzo[1,2-c:4,5-c']dithiophene-4,8-dione and benzothiadiazole units. Polym. (United Kingdom) 148, 330–338. https://doi.org/10.1016/j.polymer.2018.06.038.

Kwon, S., Kang, H., Lee, J.-H., Lee, J., Hong, S., Kim, H., Lee, K., 2017. Effect of processing additives on organic photovoltaics: recent progress and future prospects. Adv. Energy Mater. 7, 1601496. https://doi.org/10.1002/aenm.201601496.

Kwon, S., Park, J.K., Kim, J., Kim, G., Yu, K., Lee, J., Jo, Y.R., Kim, B.J., Kang, H., Kim, J., Kim, H., Lee, K., 2015. In situ studies of the molecular packing dynamics of bulk-heterojunction solar cells induced by the processing additive 1-chloronaphthalene. J. Mater. Chem. A 3, 7719–7726. https://doi.org/10.1039/c5ta00833f.

Lee, B.H., Lee, J.H., Jeong, S.Y., Park, S.B., Lee, S.H., Lee, K., 2015. Broad work-function tunability of p-type conjugated polyelectrolytes for efficient organic solar cells. Adv. Energy Mater. 5, 1–5. https://doi.org/10.1002/aenm.201401653.

Lee, E.J., Heo, S.W., Han, Y.W., Moon, D.K., 2016a. An organic-inorganic hybrid interlayer for improved electron extraction in inverted polymer solar cells. J. Mater. Chem. C 4, 2463–2469. https://doi.org/10.1039/c5tc03754a.

Lee, J.H., Kim, K.M., Jang, W., Ahn, S., Kim, Y.Y., Park, O.O., Wang, D.H., 2017. Vacuum-process-based dry transfer of active layer with solvent additive for efficient organic photovoltaic devices. J. Mater. Chem. C 5, 1106–1112. https://doi.org/10.1039/c6tc04743b.

Lee, J.K., Ma, W.L., Brabec, C.J., Yuen, J., Moon, J.S., Kim, J.Y., Lee, K., Bazan, G.C., Heeger, A.J., 2008. Processing additives for improved efficiency from bulk heterojunction solar cells. J. Am. Chem. Soc. 130, 3619–3623. https://doi.org/10.1021/ja710079w.

Lee, S., Kong, J., Lee, K., 2016b. Air-stable organic solar cells using an iodine-free solvent additive. Adv. Energy Mater. 6. https://doi.org/10.1002/aenm.201600970.

Li, J., Jian, H., Yao, L., Zhao, M., Shu, J., Xiao, X., Jiu, T., 2018. Highly efficient regular polymer solar cells based on Li-TFSI doping ZnO as electron-transporting interlayers. Sol. Energy 169, 49–54. https://doi.org/10.1016/j.solener.2018.04.018.

Liang, Q., Han, J., Song, C., Yu, X., Smilgies, D.M., Zhao, K., Liu, J., Han, Y., 2018. Reducing the confinement of PBDB-T to ITIC to improve the crystallinity of PBDB-T/ITIC blends. J. Mater. Chem. A 6, 15610–15620. https://doi.org/10.1039/c8ta05892j.

Liao, S.H., Jhuo, H.J., Cheng, Y.S., Chen, S.A., 2013. Fullerene derivative-doped zinc oxide nanofilm as the cathode of inverted polymer solar cells with low-bandgap polymer (PTB7-Th) for high performance. Adv. Mater. 25, 4766–4771. https://doi.org/10.1002/adma.201301476.

Lin, Y., Wang, J., Zhang, Z.-G., Bai, H., Li, Y., Zhu, D., Zhan, X., 2015. An electron acceptor challenging fullerenes for efficient polymer solar cells. Adv. Mater. 27, 1170–1174. https://doi.org/10.1002/adma.201404317.

Liu, F., Shao, S., Guo, X., Zhao, Y., Xie, Z., 2010. Efficient polymer photovoltaic cells using solution-processed MoO3as anode buffer layer. Sol. Energy Mater. Sol. Cells 94, 842–845. https://doi.org/10.1016/j.solmat.2010.01.004.

Liu, X., Xie, B., Duan, C., Wang, Z., Fan, B., Zhang, K., Lin, B., Colberts, F.J.M., Ma, W., Janssen, R.A.J., Huang, F., Cao, Y., 2018. A high dielectric constant non-fullerene acceptor for efficient bulk-heterojunction organic solar cells. J. Mater. Chem. A 6, 395–403. https://doi.org/10.1039/c7ta10136h.

Lou, S.J., Szarko, J.M., Xu, T., Yu, L., Marks, T.J., Chen, L.X., 2011. Effects of additives on the morphology of solution phase aggregates formed by active layer components of high-efficiency organic solar cells. J. Am. Chem. Soc. 133, 20661–20663. https://doi.org/10.1021/ja2085564.

Ma, W., Yang, C., Gong, X., Lee, K., Heeger, A.J., 2005. Thermally stable, efficient polymer solar cells with nanoscale control of the interpenetrating network morphology. Adv. Funct. Mater. 15, 1617–1622. https://doi.org/10.1002/adfm.200500211.

Meng, D., Sun, D., Zhong, C., Liu, T., Fan, B., Huo, L., Li, Y., Jiang, W., Choi, H., Kim, T., Kim, J.Y., Sun, Y., Wang, Z., Heeger, A.J., 2016. High-performance solution-processed non-fullerene organic solar cells based on selenophene-containing perylene bisimide acceptor. J. Am. Chem. Soc. 138, 375–380. https://doi.org/10.1021/jacs.5b11149.

Moulé, A.J., Meerholz, K., 2009. Morphology control in solution-processed bulk-heterojunction solar cell mixtures. Adv. Funct. Mater. 19, 3028–3036. https://doi.org/10.1002/adfm.200900775.

Oseni, S.O., Mola, G.T., 2017. The effect of uni- and binary solvent additives in PTB7:PC61BM based solar cells. Sol. Energy 150, 66–72. https://doi.org/10.1016/j.solener.2017.04.027.

Park, S.H., Roy, A., Beaupré, S., Cho, S., Coates, N., Moon, J.S., Moses, D., Leclerc, M., Lee, K., Heeger, A.J., 2009. Bulk heterojunction solar cells with internal quantum efficiency approaching 100%. Nat. Photonics 3, 297–303. https://doi.org/10.1038/nphoton.2009.69.

Qian, D., Ye, L., Zhang, M., Liang, Y., Li, L., Huang, Y., Guo, X., Zhang, S., Tan, Z., Hou, J., 2012. Design, application, and morphology study of a new photovoltaic polymer with strong aggregation in solution state. Macromolecules 45, 9611–9617. https://doi.org/10.1021/ma301900h.

Qin, M., Cheng, P., Mai, J., Lau, T.-K., Zhang, Q., Wang, J., Yan, C., Liu, K., Su, C.-J., You,

W., Lu, X., Zhan, X., 2017. Enhancing efficiency and stability of organic solar cells by UV absorbent. Sol. RRL 1700148, 1700148. https://doi.org/10.1002/solr.201700148.

Ren, G., Ahmed, E., Jenekhe, S.A., 2011. Non-fullerene acceptor-based bulk heterojunction polymer solar cells: engineering the nanomorphology via processing additives. Adv. Energy Mater. 1, 946–953. https://doi.org/10.1002/aenm.201100285.

Sai-Anand, G., Dubey, A., Gopalan, A.-I., Venkatesan, S., Ruban, S., Reza, K.M., Choi, J., Lakhi, K.S., Xu, B., Qiao, Q., Vinu, A., 2018. Additive assisted morphological optimization of photoactive layer in polymer solar cells. Sol. Energy Mater. Sol. Cells 182, 246–254. https://doi.org/10.1016/j.solmat.2018.03.031.

Sánchez, J.G., Balderrama, V.S., Estrada, M., Osorio, E., Ferré-Borrull, J., Marsal, L.F., Pallarès, J., 2017. Stability study of high efficiency polymer solar cells using TiOxas electron transport layer. Sol. Energy 150, 147–155. https://doi.org/10.1016/j.solener.2017.04.013.

Song, X., Gasparini, N., Baran, D., 2018. The influence of solvent additive on polymer solar cells employing fullerene and non-fullerene acceptors. Adv. Electron. Mater. 4, 1–7. https://doi.org/10.1002/aelm.201700358.

Sun, Q., Zhang, F., An, Q., Zhang, M., Ma, X., Zhang, J., 2017. Simultaneously enhanced efficiency and stability of polymer solar cells by employing solvent additive and upside-down drying method. ACS Appl. Mater. Interfaces 9, 8863–8871. https://doi.org/10.1021/acsami.7b00510.

Tremolet De Villers, B.J., O'Hara, K.A., Ostrowski, D.P., Biddle, P.H., Shaheen, S.E., Chabinyc, M.L., Olson, D.C., Kopidakis, N., 2016. Removal of residual diiodooctane improves photostability of high-performance organic solar cell polymers. Chem. Mater. 28, 876–884. https://doi.org/10.1021/acs.chemmater.5b04346.

Wan, Q., Guo, X., Wang, Z., Li, W., Guo, B., Ma, W., Zhang, M., Li, Y., 2016. 10.8% efficiency polymer solar cells based on PTB7-Th and PC71BM via binary solvent additives treatment. Adv. Funct. Mater. 26, 6635–6640. https://doi.org/10.1002/adfm.201602181.

Wienk, M.M., Kroon, J.M., Verhees, W.J.H., Knol, J., Hummelen, J.C., van Hal, P.A., Janssen, R.A.J., 2003. Efficient methano[70]fullerene/MDMO-PPV bulk heterojunction photovoltaic cells. Angew. Chemie Int. Ed. 42, 3371–3375. https://doi.org/10.1002/anie.200351647.

Xu, W., Yan, C., Kan, Z., Wang, Y., Lai, W.Y., Huang, W., 2016. High efficiency inverted organic solar cells with a neutral fulleropyrrolidine electron-collecting interlayer. ACS Appl. Mater. Interfaces 8, 14293–14300. https://doi.org/10.1021/acsami.6b03974.

Xu, Z., Chen, L.M., Yang, G., Huang, C.H., Hou, J., Wu, Y., Li, G., Hsu, C.S., Yang, Y., 2009. Vertical phase separation in poly(3-hexylthiophene): fullerene derivative blends and its advantage for inverted structure solar cells. Adv. Funct. Mater. 19, 1227–1234. https://doi.org/10.1002/adfm.200801286.

Yan, H., Chen, J., Zhou, K., Tang, Y., Meng, X., Xu, X., Ma, W., 2018. Lewis acid doping induced synergistic effects on electronic and morphological structure for donor and acceptor in polymer solar cells. Adv. Energy Mater. 8, 1–7. https://doi.org/10.1002/aenm.201703672.

Ye, L., Jing, Y., Guo, X., Sun, H., Zhang, S., Zhang, M., Huo, L., Hou, J., 2013. Remove the residual additives toward enhanced efficiency with higher reproducibility in polymer solar cells. J. Phys. Chem. C 117, 14920–14928. https://doi.org/10.1021/jp404395q.

Ye, L., Zhang, S., Ma, W., Fan, B., Guo, X., Huang, Y., Ade, H., Hou, J., 2012. From binary to ternary solvent: morphology fine-tuning of D/A blends in PDPP3T-based polymer solar cells. Adv. Mater. 24, 6335–6341. https://doi.org/10.1002/adma.201202855.

Yu, J.E., Jeon, S.J., Choi, J.Y., Han, Y.W., Ko, E.J., Moon, D.K., 2019. A 3-Fluoro-4-hexylthiophene-based wide bandgap donor polymer for 10.9% efficiency eco-friendly nonfullerene organic solar cells. Small 1805321, 1805321. https://doi.org/10.1002/smll.201805321.

Zhao, J., Li, Y., Yang, G., Jiang, K., Lin, H., Ade, H., Ma, W., Yan, H., 2016a. Efficient organic solar cells processed from hydrocarbon solvents. Nat. Energy 1.

Zhao, W., Qian, D., Zhang, S., Li, S., Inganas, O., Cao, F., Hou, J., 2016b. Fullerene-free polymer solar cells with over 11% efficiency. Adv. Mater. 4734–4739. https://doi.org/10.11777/j.issn1000-3304.2016.16111.

Zheng, Y., Goh, T., Fan, P., Shi, W., Yu, J., Taylor, A.D., 2016. Toward efficient thick active PTB7 photovoltaic layers using diphenyl ether as a solvent additive. ACS Appl. Mater. Interfaces 8, 15724–15731. https://doi.org/10.1021/acsami.6b03453.

Zheng, Y., Huang, J., Wang, G., Kong, J., Huang, D., Mohadjer Beromi, M., Hazari, N., Taylor, A.D., Yu, J., 2018. A highly efficient polymer non-fullerene organic solar cell enhanced by introducing a small molecule as a crystallizing-agent. Mater. Today 21, 79–87. https://doi.org/10.1016/j.mattod.2017.10.003.

Zhou, H., Zhang, Y., Seifter, J., Collins, S.D., Luo, C., Bazan, G.C., Nguyen, T.Q., Heeger, A.J., 2013. High-efficiency polymer solar cells enhanced by solvent treatment. Adv. Mater. 25, 1646–1652. https://doi.org/10.1002/adma.201204306.